A Parameter Sweep Experiment on Quasi-Periodic Variations of a Polar Vortex due to Wave-Wave Interaction in a Spherical Barotropic Model

Yasuko Hio and Shigeo Yoden [1]

Department of Geophysics, Kyoto University, Kyoto, Japan

revised

January 31, 2007

[1] *Corresponding author address:* Shigeo Yoden, Department of Geophysics, Kyoto University, Kyoto, 606-8502, Japan. E-mail: yoden@kugi.kyoto-u.ac.jp

Abstract

Weakly nonlinear aspects of a barotropically unstable polar vortex in a forced-dissipative system with a zonally asymmetric surface topography are investigated in order to obtain deeper understanding of rather periodic variations of the winter circumpolar vortex in the Southern Hemisphere stratosphere, which are characterized by the wave-wave interaction between the stationary planetary wave of zonal wavenumber 1 (denoted as Wave 1) and the eastward traveling Wave 2 as studied by Hio and Yoden in 2004. We use a spherical barotropic model with a forcing of zonally symmetric jet, dissipation, and sinusoidal surface topography. We perform a parameter sweep experiment by changing the amplitude of the surface topography which forces the stationary Wave 1 and the width of the prescribed zonally symmetric jet which controls the barotropic instability to generate the traveling Wave 2. Several types of solutions from a time-independent solution to non-periodic irregular solution are obtained for the combination of these external parameters, but the predominant one obtained in a wide parameter space is periodic solution.

Details of the wave-wave interactions are described for the transition from a quasi-periodic vacillation to a periodic solution as the increase of the amplitude of topography. Phase relationships are locked at the transition, and variations of zonal mean zonal flow and topographically forced Wave 1 synchronize with periodic progression of Wave 2 in the periodic solution. A diagnosis with a low-order "empirical mode expansion" of the vorticity equation gives a limited number of dominant nonlinear triad interactions among the zonal mean, Wave 1, and Wave 2 components around the transition point.

1 Introduction

This paper considers nonlinear dynamics of an idealized winter polar vortex in the Southern Hemisphere (SH) stratosphere with a barotropic model on a spherical domain. The SH polar vortex is stronger and less disturbed compared to that of the Northern Hemisphere. In other words, the zonal mean zonal flow is stronger and planetary waves are weaker in the SH due to weaker forcing of the planetary waves in the troposphere. As a result, major stratospheric sudden warming event had not been observed in the SH before 2002 (e.g., Baldwin et al. 2003). On the other hand, rather periodic variations of the polar vortex, which are characterized by eastward rotation of the elongated polar vortex and change in the shape with a period of about a week or so, are often observed in the SH as analyzed in our previous paper (Hio and Yoden 2004, hereafter referred to as HY04). These features in the SH stratosphere are indicative of weakly nonlinear nature of the polar vortex in the SH.

The wave-wave interaction between the stationary "planetary wave of zonal wavenumber 1" (hereafter denoted as "Wave 1") and eastward propagating Wave 2 was investigated in HY04 with the NCEP/NCAR reanalysis dataset over 20 years. The stationary Wave 1 is generated in the troposphere mainly by zonally asymmetric lower boundary conditions and has significant interannual variations (Hio and Hirota 2002). On the other hand, barotropic/baroclinic instabilities of the polar night jet play an important role for the generation of the eastward propagating Wave 2 in late winter (e.g., Manney et al. 1991). The correspondence of negative or nearly zero meridional gradient of the zonal mean potential vorticity to large-amplitude events of eastward propagating Wave 2 shown by HY04 (their Fig. 15 b) suggests in situ instability of the zonal mean zonal flow as the

generation process. A typical case analyzed in HY04 shows that the transient Wave 1 generated by the wave-wave interaction has comparable amplitude to those of the stationary Wave 1 and the traveling Wave 2, and has a node around 60° S where these primary waves have large amplitudes. The transient Wave 1 travels eastward with the same angular frequency as that of the traveling Wave 2. The zonal mean polar night jet also oscillates with the same frequency such that it has its minimum when the stationary Wave 1 and the transient Wave 1 are in phase at the polar side of the node.

HY04 also discussed similar wave-wave interactions in another case in August and September 2002, before the unprecedented major stratospheric sudden warming event in the SH. Generally such wave-wave interactions in these months are not as clear as those in late winter due to slower phase speed of traveling Wave 2. However, the situation was exceptional in the mid winter in 2002 because the seasonal march was much earlier than the other years (Hio and Yoden 2005).

In HY04, similar periodic variations of the polar vortex were also obtained in a numerical experiment with a spherical barotropic model in which the stationary Wave 1 was forced by surface topography while the eastward propagating Wave 2 was generated by the barotropic instability of a forced zonally symmetric polar night jet. The model is identical to that developed by Ishioka and Yoden (1995, hereafter IY95), if the surface topography is removed. IY95 investigated the flow regimes for two barotropically unstable jet profiles introduced by Hartmann (1983), by changing three parameters which control the intensity, width, and latitudinal position of the polar night jet. They obtained quasi-periodic vacillation solutions and non-periodic irregular solutions as well as periodic steady-wave solutions in some parameter ranges.

Such single layer models have been used by some others to study fundamental dynamics

of the winter stratosphere polar vortex; such as planetary wave breaking (e.g., Juckes and McIntyre 1987, Yoden and Ishika 1993, Thuburn and Lagneau 1999), equilibrium states of initially barotropically unstable polar vortices (Prieto and Schubert 2001), and chaotic mixing process and transport barrier (Mizuta and Yoden 2001). Recently, Rong and Waugh (2004) investigated internal variations of the polar vortex in a shallow water model with planetary-scale wave forcing by surface topography and relaxation to a prescribed zonally symmetric equilibrium state. Only weak disturbances on the edge of the polar vortex were obtained for small topographic height, whereas full cycles of the breakdown and recovery of the polar vortex were obtained for large topographic height.

Following the two papers of IY95 and HY04, this work aims to investigate the flow regimes in the same model as HY04 for a wide range of the external parameters that give the amplitude of surface topography and the width of the polar night jet. The former controls the magnitude of forced stationary wave, while the latter influences on the magnitude of barotropic instability. We perform over 150 runs of the numerical time-integrations for the parameter sweep to show the predominance of the periodic solutions due to wave-wave interactions. The dynamical situation of the polar vortex is close to that of Rong and Waugh (2004) for small topographic height without breakdown of the polar vortex. In such a situation, the eastward propagating Wave 2 generated by the barotropic instability as well as the topographically forced Wave 1 plays a crucial role through the wave-wave interactions.

Steady-wave solution in the case without topography is a simple periodic solution in which Wave 2 propagates eastward with a constant phase speed, while periodic solution in the case with topography is complicated by the wave-wave interactions, because all the components must synchronize with the same frequency. In order to understand the

complicated periodic solution and vacillation further, we investigate transitions between these solutions thoroughly, because time variations are generally simpler around transition points due to small amplitude of perturbations. A low-order "empirical mode expansion" of the two-dimensional vorticity equation is introduced to diagnose the wave-wave interactions in the parameter range around the transitions of flow regime.

The model and experimental procedure are described in Section 2. Dependence of flow regime on the external parameters is shown in Section 3. Some examples of the transition of flow regime, e.g., from a periodic solution to a quasi-periodic vacillation, are examined in Section 4. Discussion is in Section 5 and concluding remarks are in Section 6.

2 Model and experimental procedure

We use the same dynamical model as in HY04 which describes two-dimensional flow on the Earth with the forcing of zonal mean zonal flow, dissipation and surface topography. The flow is governed by a potential vorticity (hereafter PV) equation in the form

$$\frac{Dq}{Dt} = -\alpha \left(\zeta - \overline{\zeta}_f\right) + \nu \left(\nabla^2 + \frac{2}{a^2}\right) \left(\zeta - \overline{\zeta}_f\right), \tag{1}$$

where $q = \zeta + f + (fh/H)$ is the PV, $\zeta = \nabla^2\psi$ is the relative vorticity, $\psi(\lambda, \phi, t)$ the streamfunction, λ the longitude, ϕ the latitude, t the time, a the radius of the Earth, $f = 2\Omega \sin\phi$ the Coriolis parameter, Ω the angular speed of the Earth's rotation, h the height of the surface topography, and H the mean depth of the fluid layer. The right hand side of Eq. (1) gives non-conservative terms, and $\overline{\zeta}_f$ is the prescribed vorticity for the forcing of zonal mean zonal flow. The relaxation time α^{-1} of the Newtonian-type forcing is set to 10 days and artificial viscosity coefficient ν is fixed at a small constant ($= 6.43 \times 10^4$ m^2 s^{-1}) to give the dissipation. The material derivative operator D/Dt and

the horizontal Laplacian operator ∇^2 are given by

$$\frac{D}{Dt} = \frac{\partial}{\partial t} + \mathbf{u}\cdot\nabla = \frac{\partial}{\partial t} + \frac{u}{a\cos\phi}\frac{\partial}{\partial\lambda} + \frac{v}{a}\frac{\partial}{\partial\phi}, \tag{2}$$

$$\nabla^2 = \left[\frac{1}{a^2\cos^2\phi}\frac{\partial^2}{\partial\lambda^2} + \frac{1}{a^2\cos\phi}\frac{\partial}{\partial\phi}\left(\cos\phi\frac{\partial}{\partial\phi}\right)\right], \tag{3}$$

respectively, where the horizontal velocity $\mathbf{u}$ is

$$\mathbf{u} = (u, v) = \left(-\frac{1}{a}\frac{\partial\psi}{\partial\phi},\ \frac{1}{a\cos\phi}\frac{\partial\psi}{\partial\lambda}\right). \tag{4}$$

The prescribed vorticity for the forcing, $\overline{\zeta}_f = -(1/a)(\partial\overline{u}_f/\partial\phi)$, is set to satisfy the necessary condition of barotropic instability (Hartmann 1983):

$$\overline{u}_f = \frac{U}{2}\left(1 + \tanh\frac{\phi-\phi_0}{B}\right)\cos\phi, \tag{5}$$

where U is a measure of the intensity of the prescribed zonally symmetric jet, B its width, and ϕ_0 its latitudinal position. All the conditions are the same as in IY95 for the case of $h = 0$, and the regime diagram for this case in the three dimensional parameter space (U, B, ϕ_0) is given in IY95 (their Fig. 1). In this work we sweep the parameter B for $3^\circ \le B \le 18^\circ$ with fixed values of $U = 240$ ms^{-1} and $\phi_0 = 55^\circ$. Eastward propagating Wave 2 is generated when B is so small, or the prescribed jet is so narrow, as to satisfy the condition of barotropic instability. Thus, sweeping the parameter B means the change of the features of the eastward propagating Wave 2.

To force stationary Wave 1, sinusoidal surface topography of zonal wavenumber 1 is assumed in the model SH as

$$h(\lambda,\phi) = \frac{1}{2}h_0(\sin 2\phi)^2\cos\lambda, \tag{6}$$

and no topography in the NH. We sweep the parameter $r = h_0/H$ for $0 \le r \le 0.1$ to investigate dynamical features depending on the forced stationary Wave 1.

We use a spectral model with a triangular truncation of T85 in spherical harmonics and the fourth-order Runge-Kutta method for time integrations, as in IY95, Mizuta and Yoden (2001), and HY04.

3 Flow regimes

3.1 Dependence on B and r

Table 1 is a regime diagram which shows the dependence of flow regime on the width of the prescribed zonally symmetric jet for $3^\circ \leq B \leq 18^\circ$ and the ratio of the topographic height to the mean fluid depth for $0 \leq r \leq 0.1$. Table 1

In the case of $r = 0$ without topography on the first row in Table 1, we obtain a time-independent solution with no wave (as denoted by N) for wide jets of $B \geq 12^\circ$. The prescribed jet becomes barotropically unstable for $B < 12^\circ$, and we obtain a steady-wave solution (S) for $6^\circ \leq B \leq 11^\circ$. In the steady-wave solution, Wave 2 travels eastward with a constant phase speed without changing its horizontal structure, and the streamfunction for this component is expressed as

$$\text{(Steady-wave)}: \quad \psi_2(\lambda, \phi, t) = C_2(\phi) e^{i(2\lambda - \omega_P t)}, \tag{7}$$

where a subscript number indicates the zonal wavenumber s. This is a periodic solution with an angular frequency ω_P.

In IY95, steady-wave solutions were obtained for $B = 8^\circ$ and 6°, while vacillation solution was obtained for $B = 4^\circ$ in which the elongated polar vortex with Wave 2 component rotates eastward by changing its shape periodically. See Fig. 4 in IY95 for the time variation of the PV field for $r = 0$. Vacillation solution (V_0) is quasi-periodic

with two incommensurable frequencies of the rotation, ω_P, and shape change, ω_A:

$$\text{(Vacillation)}: \quad \psi_2(\lambda,\phi,t) = \{C_2(\phi) + A_2(\phi)e^{i\omega_A t}\}e^{i(2\lambda-\omega_P t)}. \tag{8}$$

Table 1 shows the transition from steady-wave solution (S) to vacillation (V_0) takes place between $B = 6°$ and $5.5°$. Figure 1 shows the wave decomposition of the PV field of a vacillation solution for $B = 4°$. Time averaged structure of the traveling Wave 2, $C_2(\phi)e^{i2\lambda}$, which has an angular frequency of $\omega_P = 2\pi/10.8$ day^{-1}, is displayed in the bottom right panel. The amplitude modulation of the Wave 2 field, $A_2(\phi)e^{i\omega_A t}e^{i(2\lambda-\omega_P t)}$, is shown for 10.8 days with a time interval of 1.8 days. The pattern at $t = 0$ day and that at $t = 1.8$ day are about the same as those at $t = 9.0$ day and $t = 10.8$ day, respectively, except for the longitudinal phase. Spectral analysis shows that the frequency of the amplitude modulation is $\omega_A = 2\pi/9.2$ day^{-1} (see Fig. 6).

Fig. 1

In the cases with topography ($r \neq 0$), four kinds of solutions are obtained as shown in Table 1; stationary-wave solution (Sta), periodic solution (P), vacillation solution (V), and irregular solution (I). For wide jets of $B \geq 9°$, stationary-wave solution (Sta) is obtained, which is a time-independent solution with forced stationary Wave 1:

$$\text{(Stationary-wave)}: \quad \psi_1(\lambda,\phi) = S_1(\phi)e^{i\lambda}. \tag{9}$$

As B is reduced, transition from stationary-wave solution (Sta) to periodic solution (P) takes place for $8° < B < 9°$. The value of B for the first transition associated with the barotropic instability of the zonal jet influenced by stationary Wave 1 is reduced largely by the existence of the surface topography, although the value for the transition is not dependent on r for $0.02 \leq r \leq 0.1$. As described in detail by HY04 in their Section 3, periodic variation of the polar vortex occurs as a result of the interaction between the topographically forced Wave 1 and the traveling Wave 2 due to barotropic instability of

the prescribed jet. The streamfunctions for Wave 1 and 2 are expressed as

$$\text{(Periodic solution)}: \quad \psi_1(\lambda,\phi,t) = S_1(\phi)e^{i\lambda} + \{C_1(\phi) + B_1(\phi)e^{i\omega_B t}\}e^{i(\lambda-\omega_B t)}, \quad (10)$$

$$\psi_2(\lambda,\phi,t) = S_2(\phi)e^{i2\lambda} + \{C_2(\phi) + B_2(\phi)e^{i\omega_B t}\}e^{i(2\lambda-\omega_B t)}, \quad (11)$$

respectively. Note that these traveling waves have the same angular frequency as that of the amplitude modulation of these waves, ω_B. The zonal mean zonal flow also oscillates with the same frequency due to periodic variation of the wave driving by the interference between the stationary Wave 1 and the traveling Wave 1. Figure 2 (a) and (c) show the time mean structures of traveling Wave 2, $C_2(\phi)e^{i2\lambda}$, and traveling Wave 1, $C_1(\phi)e^{i\lambda}$, respectively, while (b) shows the structure of stationary Wave 1, $S_1(\phi)e^{i\lambda}$. The traveling Wave 2 and the stationary Wave 1 are mostly confined between 50°S and 70°S with the maximum amplitude around 63°S, while the traveling Wave 1 has the maximum around 67°S and has a node around 60°S with the secondary maximum around 55°S.

Fig. 2

Vacillation solution (V) is quasi-periodic with two incommensurable frequencies as in the case without topography (V_0), but the time variations of each component are complicated by the interactions with forced stationary Wave 1 as analyzed in the rest of this paper. Transition from periodic solution (P) to vacillation (V) takes place between $B = 3.5°$ and $4°$ for $r = 0.02$. There is no vacillation solution between $B = 4°$ and $5.5°$ in the case $r \neq 0$ in Table 1 at an interval of $\Delta r = 0.02$, but it does exist for this range of B. One can obtain vacillation solution for finite values of $r < 0.02$. Non-periodic irregular solutions (I) are obtained for $r = 0.08$ and 0.1 with small B. The interval Δr in Table 1 is too large for us to discuss the transition from periodic solution to irregular one. Similar spatial structures of Wave 1 and 2 as those shown in Fig. 2 for a periodic solution are still obtained in the irregular solutions. The similarity of the wave structures is indicative that

the wave-wave interactions are common features for a wide range of $r \neq 0$ and $B \leq 8°$ in Table 1.

3.2 Regime transitions at $B = 4°$

We now examine the regime transitions in more detail at $B = 4°$, regimes at which are denoted with bold characters in Table 1, by changing r with smaller intervals ($\Delta r = 0.001$ for $0 \leq r \leq 0.042$ and $\Delta r = 0.002$ for $0.044 \leq r \leq 0.09$). As shown in the bottom part of Fig. 3 (a), we have vacillation solutions (V) for $0 \leq r \leq 0.015$, periodic solutions (P) for $0.016 \leq r \leq 0.078$, and irregular solutions (I) for $0.08 \leq r$. Figure 3 shows the dependence on the parameter r of some quantities associated with (a) the zonal mean zonal flow, (b) Wave 2, and (c) Wave 1, at $\phi = 62.3°$S. A dot denotes the time averaged value of a quantity and accompanying vertical bar denotes its variation range. Fig. 3

The time averages of (a) the zonal mean zonal flow and (b) the amplitude of traveling Wave 2 decrease a little as r increases in the vacillation regime. Their variation ranges also gradually decrease with r. As shown in the enlargement in Fig. 3 (c), the time averaged amplitude of traveling Wave 1 increases almost linearly with r, while its variation range has a maximum around $r = 0.01$. The amplitude of stationary Wave 1 is zero when $r = 0$ and increases almost linearly with r while that of the stationary Wave 2 is quite small in the vacillation regime, as shown by the solid lines in Fig. 3 (c) and (b), respectively.

All the variation ranges of the mean zonal flow and traveling Wave 1 and 2 become smallest around $r = 0.015$ where the transition between vacillation solution and periodic solution takes place. The variation ranges of the mean zonal flow and traveling Wave 1 increase gradually and smoothly in the periodic solution regime. They become larger and more sensitively dependent on r after the transition to irregular solution at $r \simeq 0.08$

because of the chaotic nature of irregular solutions. On the other hand, the variation range of traveling Wave 2 increases for $0.015 \leq r \leq 0.052$ and then decreases to have a local minimum at $r = 0.068$. It increases again and has large values after the transition to irregular solution.

The time mean of the mean zonal flow decreases gradually as r increases, and that of traveling Wave 2 decreases over 1/2 in the range of r shown in Fig. 3. On the other hand, the time mean of traveling Wave 1 increases in this range. The stationary Wave 2 attains significant amplitude in the periodic solution regime and has a maximum at $r = 0.052$.

3.3 Synchronization in periodic solution

Figure 4 shows some examples of the time variations of the zonal mean zonal flow and Wave 1 and 2 in each regime for 8 values of r from 0 to 0.09 indicated by downward arrows a - h in Fig. 3 (a). Top row shows the time variation of the zonal mean zonal flow at 65.1°S, while middle and bottom rows show the polar diagrams of the complex amplitude of Wave 2 and 1 such as Figs. 8 and 11 in HY04. The trajectory of each wave component of the relative vorticity $(\zeta_s(\phi_s, t)e^{is\lambda},\ s = 1, 2)$ in a Re[ζ_s] - Im[ζ_s] plane gives the time variation of its amplitude and phase by $|\zeta_s|$ and arg[ζ_s], respectively. In Fig. 4, ϕ_s is chosen as the latitude at which the traveling wave component has the maximum amplitude, and the value of ϕ_s is shown in each panel. To know the phase relationship of these variations, open circle ($\circ$) or plus sign ($+$) is put at each timing when the zonal mean zonal flow has a local maximum or minimum value.

Fig. 4

In the vacillation solution without topography, the zonal mean zonal flow varies purely periodically and the polar diagram of Wave 2 shows torus structure as shown in Fig. 4 (a). The torus structure is unique for vacillation and it reflects the modulation of wave

amplitude without preference or dependence on the wave phase. Note that the open circles are on the inner side of the torus while the plus signs on the outer side. This relationship means small (large) amplitude of Wave 2 for maximum (minimum) value of the mean zonal flow. The polar diagram of Wave 1 has no amplitude for $r = 0$, while it shows coexistence of the stationary and traveling components for $r \neq 0$. The stationary component is denoted by a small dot in each panel, while the traveling one is recognized as the vector difference between a point on the trajectory and the stationary component. Thickness of the torus for Wave 2 gets thinner with r, corresponding to the decrease of the variation range of traveling Wave 2 as shown in Fig. 3 (b).

It is very difficult to distinguish deformation of the vacillation solution due to the existence of surface topography in Fig. 4 (b) and (c) except for the polar diagram of Wave 1, but the deformation becomes clear for larger r just before the transition to periodic solution as shown in Fig. 5 for $r = 0.0145$ (a), 0.015 (b), and 0.01502 (c). A periodic solution shown in Fig. 5 (d) is obtained for $r = 0.01504$ after the transition. The transition point exists between $r = 0.01502$ and 0.01504. Beat of the fluctuation of the zonal mean zonal flow is seen for vacillation solutions; the modulation becomes small in (c) and is not found in (d). The timings when the mean zonal flow has its local maximum (open circle) or minimum (plus sign) are not very relevant to the phases of Wave 2 and 1 at $r = 0.0145$ (a), while the timings have preferred phase both in Wave 2 and 1 for $r = 0.015$ (b) and 0.01502 (c). The variation range of the phases denoted by open circle or plus sign becomes small as r increases to the transition point, and the timings is completely locked for the periodic solution (d). In other words, fluctuations of the zonal mean zonal flow and topographically forced Wave 1 synchronize with periodic progression of Wave 2 in the periodic solution. These features of the periodic solution

Fig. 5

remain in the vacillation solutions in the vicinity of the transition point as the preferred phase relationship. Variations of the mean zonal flow and amplitudes of Waves 1 and 2 become rather independent from the progression of Wave 2 in the vacillation solutions as r is further reduced.

Around the transition point from vacillation to periodic solution ($r = r_b \simeq 0.01503$), the orbits of Wave 2 and 1 in the polar diagrams become nearly circular in consistent with the minima of the variation ranges of the Wave 2 and 1 as shown in Fig. 3. In Fig. 4 (d) for $r = 0.016$, a perfect circle is drawn by dashed line to show the smallness of the deviation of the periodic orbit from the steady wave with a constant amplitude. As r increases, the deviation of the orbits from a circle becomes discernible in Fig. 4 (f) and (g). The timings when the mean zonal flow has its local maximum or minimum delay in the phase variations of Wave 2 and 1, as indicated by the counterclockwise shifts of open circles or plus signs from (d) to (g). The phase relationships between the mean zonal flow and traveling waves for large r as (g) are similar to those shown in HY04 for $B = 6^\circ$ and $r = 0.08$: The traveling Wave 1 is almost in phase in longitude with the stationary Wave 1 and traveling Wave 2 at the timing when the mean zonal flow has its minimum value.

Even in the irregular solution (h) for $r = 0.09$, the mean zonal flow fluctuates rather periodically, and the trajectories of Wave 2 and 1 in the polar diagrams show systematic variations associated with eastward propagation of these waves.

The clustering of the symbols indicates that the synchronized phase relationships in the periodic solutions just before the transition remain in this irregular solution.

3.4 Power spectra

Power spectral analysis is done to examine the periodic, quasi-periodic, or non-periodic nature quantitatively in the three regimes obtained in the previous subsection.

Figure 6 shows three power spectral densities for the following time series of six solutions from (a) - (h) given in Figs. 4; (top) the zonal mean relative vorticity, $\zeta_0(\phi_0 = 62.3°\mathrm{S}, t)$, (middle) the amplitude of Wave 2 vorticity, $|\zeta_2(\phi_2 = 62.3°\mathrm{S}, t)|$, and (bottom) the Wave 2 vorticity component at a given point $(\lambda_2, \phi_2) = (0°, 62.3°\mathrm{S})$ which contains the wave phase information, $\mathrm{Re}[\ \zeta_2(\phi_2, t)e^{i2\lambda_2}\ ]$. Fig. 6

For the vacillation solution (a) without surface topography (V_0 with $r = 0$), both time series of the zonal mean and the amplitude of Wave 2 have spectral peaks at the frequency of $f_A = 2\pi\omega_A = 0.112$ day^{-1} and its higher harmonics. On the other hand, the power spectral density for the Wave 2 component at a given point has the largest peak at $f_B = 2\pi\omega_B = 0.0927$ day^{-1} and other peaks at the linear combination frequencies of f_A and f_B. These frequencies of the amplitude modulation and the phase propagation of Wave 2 are incommensurable, so that the polar diagram in Fig. 4 (a) has the torus structure; this is a fundamental property of quasi-periodic solutions.

The vacillation solutions in the presence of the surface topography (V) have spectral peaks at f_A, f_B, and their linear combinations in all the three power spectra, as shown in Fig. 6 (b) and (c). The frequency f_B corresponding to wave propagation is dominant in the time series at a given point, while the other frequency f_A is dominant in the spectra of the zonal mean and Wave 2 amplitude for $r = 0.008$ (b). The power at the wave propagation frequency f_B dominates even in the time series of the zonal mean for $r = 0.014$ (c).

For the periodic solutions (P), the flow field changes purely periodically at the fre-

quency f_B of the phase propagation of Wave 2, and thus all the spectra have peaks at the frequencies of f_B and its higher harmonics as shown for $r = 0.016$ (d) and $r = 0.070$ (g). Irregular solutions (I) have continuous power spectra with increased power at all the frequencies as shown in Fig. 6 (h) for $r = 0.09$. However, spectral peaks still exist around the frequency f_B ($\sim 0.11\text{day}^{-1}$) of the periodic solutions, indicating that the fundamental feature of the periodic solutions remains in some degree in the irregular solution.

In order to see the variations of the dominant spectral peaks with r more quantitatively, we show frequency of power spectral peaks in Fig. 7 (top) and corresponding power spectral density (bottom) for only three components of f_A, f_B, and $f_A - f_B$ which are obtained from the time series of (a) the zonal mean component, (b) the amplitude of Wave 2, and (c) the amplitude of Wave 1, of the relative vorticity at $\phi = 62.3°\text{S}$. The frequencies of the dominant peaks of the power spectra do not change very much in the range of $0 \leq r \leq 0.02$. The vacillation solution (V_0) for $r = 0$ has a spectral peak only at f_A, and periodic solutions for $r > r_b \simeq 0.01503$ have a spectral peak only at f_B. On the other hand, another type of vacillation (V) in the presence of the surface topography ($r \neq 0$) has the spectral peaks at the three frequencies, f_A, f_B, and $f_A - f_B$.

Fig. 7

Variations of the power spectral densities for these frequencies with r are very similar between (a) the zonal mean component and (b) the amplitude of Wave 2. As r increases from zero, the power spectral density for f_A decreases gradually while that for f_B increases much sharply from zero. These two components becomes comparable magnitude around $r \sim 0.0145$, and then the power for f_A decreases very sharply to zero as r approaches the transition point, or the bifurcation point of quasi-periodic solution from periodic solution, at $r = r_b \simeq 0.01503$. The power for f_B increases continuously as r increases beyond r_b. The power spectral densities for these frequencies show a different dependence on r for

the time series of the amplitude of Wave 1 (c).

4 Diagnosis on regime transitions

As shown in Figs. 6 and 7, some qualitative changes in the time variations of the zonal mean component and amplitudes of Wave 1 and 2 take place around $r = 0$ and r_b. The zonal symmetry of the external conditions breaks when the surface topography is introduced, no matter how r is small. This symmetry breaking of the external forcing brings a qualitative change in the vacillation solutions from V_0 to V. On the other hand, there is no symmetry breaking of the external forcing around r_b, but the transition from periodic solution (P) to quasi-periodic vacillation (V) takes place. In this section, these regime transitions are diagnosed from the viewpoint of wave-wave interactions based on a low-order "empirical mode expansion" of the vorticity equation to understand the fundamental properties of time variations of these solutions.

4.1 A low-order "empirical mode expansion"

In the parameter range described in the previous section, the flow is weakly nonlinear such that interactions between the zonal mean zonal flow and a limited number of dominant waves, Wave 1 and 2, determine the time variations of the flow field. If we expand a dependent variable as $X(\lambda, \phi, t) = \sum_{s=0}^{2} X_s(\phi, t) e^{is\lambda}$ and substitute them into the PV equation (1), we finally obtain the zonal mean, Wave 1, and Wave 2 components of that

equation as follows,

$$\frac{\partial q_0}{\partial t} = -\left\{\frac{1}{a}\frac{\partial}{\partial\phi}(v_1 q_1) + \frac{1}{a}\frac{\partial}{\partial\phi}(v_2 q_2)\right\}_0, \tag{12}$$

$$\frac{\partial q_1}{\partial t} + \frac{u_0}{a\cos\phi}\frac{\partial q_1}{\partial\lambda} + \frac{v_1}{a}\frac{\partial q_0}{\partial\phi} = -\left\{\nabla\cdot(\mathbf{u}_1 q_2) + \nabla\cdot(\mathbf{u}_2 q_1)\right\}_1, \tag{13}$$

$$\frac{\partial q_2}{\partial t} + \frac{u_0}{a\cos\phi}\frac{\partial q_2}{\partial\lambda} + \frac{v_2}{a}\frac{\partial q_0}{\partial\phi} = -\left\{\nabla\cdot(\mathbf{u}_1 q_1)\right\}_2, \tag{14}$$

after neglecting the source and sink terms on the right hand side of Eq. (1).

Because the patterns of time variations of the zonal mean zonal flow and planetary waves have large amplitude only in high latitudes with a maximum or a node near $\phi_c = 60°$S, as shown in Fig. 2 for example, we can introduce a new meridional coordinate ϕ' to represent those with a couple of "empirical modes" as follows:

$$\phi' \simeq (\phi - \phi_c)\pi/\Delta\phi, \tag{15}$$

$$X(\lambda,\phi,t) = \sum_{s=0}^{2}\sum_{m=1}^{2} X_s^m(t) e^{i(s\lambda + m\phi')}, \tag{16}$$

where $\Delta\phi(\simeq 30°)$ is a meridional extent of the variations, s a zonal wavenumber, and m a meridional mode number.

There is no mathematical rigorousness of this low-order expansion, but we can argue triad wave interaction in the weakly nonlinear dispersion theory reviewed in HY04 more easily with a simple double Fourier expansion. Note that the expansion in spherical harmonics is not effective in the present situation because the variations are confined in middle and high latitude of a hemisphere.

For the interactions in such a low-order system obtained by a double Fourier expansion, we can rely on a classic theory on the mechanics of vacillation in a rotating annulus experiment with radial differential heating by Lorenz (1963) and the studies on the bifurcation properties of a barotropic or two-layer baroclinic flow over topography by the senior author of this paper (Yoden 1983a, b; Yoden 1985a, b).

4.2 Topographic effect on vacillation around $r = 0$

The vacillation solution (V_0) without topography at $r = 0$ is described in the low-order "empirical mode expansion" as

$$\psi_0 \simeq \psi_{o0} = C_0^1 e^{i\phi'} + A_0^2 e^{i\omega_A t} e^{i2\phi'}, \tag{17}$$

$$\psi_1 = \psi_{o1} = 0, \tag{18}$$

$$\psi_2 \simeq \psi_{o2} = \left\{ C_2^1 + A_2^1 e^{i\omega_A t} \right\} e^{i(2\lambda + \phi' - \omega_B t)}. \tag{19}$$

The components with coefficients C_0^1 and C_2^1 constitute a steady-wave solution with a constant Wave 2 propagation with angular frequency ω_B, while those with A_0^2 and A_2^1 represent the periodic variation of the flow field with another frequency ω_A. In this notation, energy exchange between the mean zonal flow (A_0^2) and Wave 2 (A_2^1) with the angular frequency ω_A takes place through the triad wave-mean flow interaction in association with the component of steady Wave 2 (C_2^1). These components satisfy three wave resonance relationship: $(0, 2) \pm (2, 1) = (2, 1)$, where (s, m) is the wavenumber vector. A schematic diagram of possible interactions between these components can be found in Fig. 1 in Yoden (1983b).

Assuming the independence of the steady-wave components on r and the linear growth of forced stationary Wave 1 with r from Fig. 3, that is,

$$|C_0^1| \propto r^0, \quad \text{and} \quad |C_2^1| \propto r^0, \tag{20}$$

$$|S_1^1| \propto r, \tag{21}$$

for small r, we can argue triad interactions which produce the modulation of vacillation due to the surface topography, and estimate the dependence of the modulation on r.

(I) The wave-wave interaction between the stationary Wave 1 (S_1^1) and the steady east-

ward traveling Wave 2 (C_2^1) with the angular frequency ω_B produces the eastward traveling Wave 1 (B_1^2) with the same frequency ω_B. As the amplitude $|B_1^2|$ is proportional to $|S_1^1||C_2^1|$ from the right-hand-side of Eq. (13), it is proportional to r from Eqs. (20) and (21). This relationship is schematically written as

$$S_1^1(\propto r)\ C_2^1(\propto r^0) \quad \Rightarrow \quad B_1^2(\propto r)e^{i(\lambda+2\phi'-\omega_B t)}, \tag{22}$$

where the inside of parentheses denotes the dependence of the amplitude on r.

(II) The interference between the stationary Wave 1 (S_1^1) and the generated traveling Wave 1 (B_1^2) produces the fluctuation of the zonal mean component (B_0^1) with the angular frequency ω_B. The amplitude $|B_0^1|$ is proportional to $|S_1^1||B_1^2|$ from the right-hand-side of Eq. (12). Thus, the term B_0^1 increases as r^2:

$$S_1^1(\propto r)\ B_1^2(\propto r) \quad \Rightarrow \quad B_0^1(\propto r^2)e^{i(\phi'+\omega_B t)}. \tag{23}$$

(III) The wave-mean flow interaction between the steady eastward traveling Wave 2 (C_2^1) and the generated zonal mean fluctuation (B_0^1) produces the second mode of eastward propagating Wave 2 (B_2^2) with amplitude modulation with the angular frequency ω_B. The amplitude $|B_2^2|$ is proportional to $|C_2^1||B_0^1|$ from the left-hand-side of Eq. (14) and increases as r^2:

$$C_2^1(\propto r^0)\ B_0^1(\propto r^2) \quad \Rightarrow \quad B_2^2(\propto r^2)e^{i\omega_B t}e^{i(2\lambda+2\phi'-\omega_B t)}. \tag{24}$$

In summary, these terms influenced by the surface topography are added to the original vacillation solution, Eqs. (17) $\sim$ (19), for small r,

$$\psi_0 \simeq \psi_{o0} + B_0^1(\propto r^2)e^{i(\phi'+\omega_B t)}, \tag{25}$$

$$\psi_1 \simeq \psi_{o1} + B_1^2(\propto r)e^{i(\lambda+2\phi'-\omega_B t)}, \tag{26}$$

$$\psi_2 \simeq \psi_{o2} + B_2^2(\propto r^2)e^{i\omega_B t}e^{i(2\lambda+2\phi'-\omega_B t)}. \tag{27}$$

In order to see the dependence on r as stated above directly, the power spectral densities for the frequencies f_A (plus sign) and f_B (closed circle) shown in Fig. 7 are replotted in Fig. 8 on a double logarithmic chart. Both of the power of the zonal mean component (a) and that of the amplitude of Wave 2 (b) for the angular frequency ω_B (closed circle) increase with r along the line r^4. On the other hand, the power of the amplitude of Wave 1 (c) for the angular frequency ω_B increases with r along the line r^2. These power laws are consistent with the above arguments, indicating both B_0^1 and B_2^2 are proportional to r^2 while B_1^2 is proportional to r. Fig. 8

4.3 Bifurcation of vacillation solution at $r = r_b$

Transition from a periodic solution (P) to vacillation (V) takes place at $r_b \simeq 0.01503$ as r is reduced from above as shown in Fig. 5. Because the external forcing is constant with time in this experiment, this could be a bifurcation of quasi-periodic solution with two incommensurable angular frequencies ω_A and ω_B from a periodic solution with ω_B. We diagnose this transition by the low-order "empirical mode expansion", describing a periodic solution above r_b as

$$\psi_0 \simeq \psi_{p0} = C_0^1(\propto r^0)e^{i\phi'} + B_0^1(\propto r^2)e^{i(\phi'+\omega_B t)}, \tag{28}$$

$$\psi_1 \simeq \psi_{p1} = S_1^1(\propto r)e^{i(\lambda+\phi')} + B_1^2(\propto r)e^{i(\lambda+2\phi'-\omega_B t)}, \tag{29}$$

$$\psi_2 \simeq \psi_{p2} = \left\{C_2^1(\propto r^0)e^{i\phi'} + B_2^2(\propto r^2)e^{i\omega_B t}e^{i2\phi'}\right\} e^{i(2\lambda-\omega_B t)}. \tag{30}$$

For $r > r_b$, these components fluctuate at the angular frequency ω_B through the wave-wave and wave-mean flow interactions as described in the previous subsection.

We assume a Hopf bifurcation at r_b. When a Hopf bifurcation takes place, generally a small amplitude limit cycle bifurcates from a fixed point of a dynamical system when

the fixed point loses stability with respect to a time-periodic perturbation. Near the bifurcation point, the amplitude of the limit cycle increases in proportion to the square root of the increment of the bifurcation parameter. In the present case, the periodic solution with a frequency ω_B becomes a fixed point after making Poincare map for the periodic orbit, so that periodic modulation with another frequency ω_A appears as a result of the Hopf bifurcation. Assuming an increase of the amplitude modulation of eastward traveling Wave 2 by the square root law as,

$$A_2^1(\propto (r_b - r)^{1/2}) e^{i\omega_A t} e^{i(2\lambda + \phi' - \omega_B t)}, \tag{31}$$

near the bifurcation point r_b with $r < r_b$, we can argue triad interactions which are associated with this amplitude modulation, and estimate the dependence of the modulation on $(r_b - r)$.

(i) The interaction between the steady eastward traveling Wave 2 (C_2^1) and the amplitude modulation of Wave 2 (A_2^1) produces the fluctuation of the zonal mean component (A_0^2) with the angular frequency ω_A. The amplitude $|A_0^2|$ is proportional to $|C_2^1||A_2^1|$ from the right-hand-side of Eq. (12). Thus, the term A_0^2 increases as $(r_b - r)^{1/2}$:

$$C_2^1(\propto r^0)\ A_2^1(\propto (r_b - r)^{1/2}) \quad \Rightarrow \quad A_0^2(\propto (r_b - r)^{1/2}) e^{i\omega_A t} e^{i2\phi'}. \tag{32}$$

(ii) The wave-wave interaction between the stationary Wave 1 (S_1^1) and the amplitude modulation of Wave 2 (A_2^1) generates the modulation of the eastward traveling Wave 1 (A_1^2) with the angular frequency ω_A. The amplitude $|A_1^2|$ is proportional to $|S_1^1||A_2^1|$

from the right-hand-side of Eq. (13), and it increases as $(r_b - r)^{1/2}$:

$$S_1^1\,(\propto (r_b - (r_b - r)))\;\; A_2^1(\propto (r_b - r)^{1/2}) \quad \Rightarrow \quad A_1^2(\propto r_b(r_b - r)^{1/2})e^{i\omega_A t}e^{i(\lambda + 2\phi' - \omega_B t)}. \tag{33}$$

In summary, these amplitude modulation terms with the angular frequency ω_A are added to the periodic solution, Eqs. (28) $\sim$ (30), for small $(r_b - r)$,

$$\psi_0 \;\simeq\; \psi_{p0} + A_0^2(\propto (r_b - r)^{1/2})e^{i\omega_A t}e^{i2\phi'}, \tag{34}$$

$$\psi_1 \;\simeq\; \psi_{p1} + A_1^2(\propto (r_b - r)^{1/2})e^{i\omega_A t}e^{i(\lambda + 2\phi' - \omega_B t)}, \tag{35}$$

$$\psi_2 \;\simeq\; \psi_{p2} + A_2^1(\propto (r_b - r)^{1/2})e^{i\omega_A t}e^{i(2\lambda + \phi' - \omega_B t)}. \tag{36}$$

To confirm this relationship, the power spectral densities for the frequency ω_A are plotted against $(r_b - r)$ for $r < r_b$ on a double logarithmic chart in Fig. 9. Fig. 9

All of the power spectral densities of the zonal mean component (a) and the amplitudes of Wave 2 (b) and Wave 1 (c) for the angular frequency ω_A increase in proportion to $(r_b - r)$ along dashed lines from the bifurcation point r_b. These power laws support that the transition from periodic solution (P) to vacillation (V) is due to the Hopf bifurcation at r_b for decreasing r.

5 Discussion

In the previous section, our attention was focused on the parameter range of small r to diagnose the regime transition, in which the forced stationary Wave 1 is much smaller than that of traveling Wave 2. In the real SH stratosphere, however, the amplitude of the stationary Wave 1 is comparable to or larger than that of the traveling Wave 2. In HY04, the periodic solution for $B = 6^\circ$ and $r = 0.08$ (denoted by P^* in Table 1) was taken as

an example similar to the observation. For the real atmosphere and the cases for large r in the present study, the periodic fluctuation of the zonal mean zonal flow is basically explained by the energy and enstrophy exchanges with Wave 1, while it is mainly due to the exchanges with Wave 2 for small r. The enstrophy exchange between the mean zonal flow and the Wave 1 becomes dominant for about $r > 0.05$ at $B = 4°$. As shown in Fig. 3, there are some systematic changes in the zonal mean zonal flow and Wave 2 around $r \sim 0.05$. The maximum value in the mean zonal flow fluctuation increases with r for $r \lesssim 0.05$ while it is roughly constant for $r \gtrsim 0.05$. The variation range of Wave 2 and the amplitude of stationary Wave 2 increase for $r \lesssim 0.05$ while these decrease for $r \gtrsim 0.05$. On the other hand, the amplitude of stationary Wave 1 and the variation range of Wave 1 increase for all the ranges shown in Fig. 3.

As analyzed for the real SH stratosphere in HY04, rather periodic variations of the polar vortex due to the wave-wave interactions are often observed in late winter, and the existence of the eastward propagating Wave 2 as well as the stationary Wave 1 is the key factor that determines whether such variations are observed or not. The large activity of the eastward traveling Wave 2 is related to a barotropically unstable profile or weakly stable one of the mean polar night jet as shown in Fig. 15 (b) in HY04. As the season evolves from early winter to late winter in the SH, the polar night jet in the middle stratosphere becomes strong due to its shift to poleward and downward (Shiotani et al. 1993). In the parameter setting for the prescribed polar night jet in the present study, $\phi_0 = 55°$ and $B = 4°$ with $r = 0$, it is barotropically stable for small U while it becomes unstable to have steady-wave solutions for $U = 180$ and 210 ms^{-1} and vacillation solutions for 240 and 270 ms^{-1} as shown in IY95. In the presence of surface topography with a finite value of r, stationary-wave solutions are obtained for barotropically stable polar night jet

with small U. The seasonal evolution of the SH middle stratosphere can be mimicked by increasing U with transitions from stationary-wave solution to irregular solution via periodic solution. In early winter eastward traveling Wave 2 is not active because of the weak polar night jet, while it becomes active in late winter and then periodic variations of the polar vortex due to the wave-wave interaction between the traveling Wave 2 and stationary Wave 1 are observed.

As shown in Figs. 1 and 2, most of the wave disturbances are confined in high latitudes for the parameter ranges of this study, even though the fluid is assumed to fill the spherical domain. Such a situation of the confinement within the polar cap is rather similar to the rotating annulus experiment with radial differential heating (e.g., Hide and Mason, 1975). Some of the laboratory experiments have been performed in order to study the wave-wave interactions between azimuthally propagating waves due to baroclinic instability and stationary waves forced by bottom topography (e.g., Li et al. 1986; Bernardet et al. 1990; Risch and Read 2005a, b). Bernardet et al. (1990) performed experiments with time independent topography of azimuthal wavenumber 2 and obtained some examples of spatial modulation of the traveling baroclinic waves and topographically induced vacillations. Although the observations of the variations of flow field in space and time were limited, the dynamical situations of these cases in the laboratory experiment may be similar to those analyzed in the present study with a low-order "empirical mode expansion". The expansion into normal modes is more rigorous for the annulus experiments, as in Lorenz's (1963) work, compared to that in this paper because of the rigid side boundaries. Further observation of the flow field in space and time in this kind of laboratory experiments with bottom topography and analysis based on the mode expansion will bring deeper understanding on the wave-wave interactions that were investigated in this study.

6 Concluding remarks

Weakly nonlinear aspects of a barotropically unstable polar vortex in a forced-dissipative system with a zonally asymmetric surface topography were investigated with a spherical barotropic model in terms of wave-wave interactions. Two experimental parameters adopted in this study are the normalized amplitude, r, of the sinusoidal surface topography of zonal wavenumber 1, which forces a stationary planetary wave of zonal wavenumber 1 (Wave 1), and the width, B, of the prescribed zonally symmetric jet, which controls the eastward propagating Wave 2 generated by the barotropic instability. A parameter sweep experiment (summarized in Table 1) showed the predominance of periodic solution in a wide parameter space. In the periodic solutions, variations of the zonal mean zonal flow and topographically forced Wave 1 synchronize with the periodic eastward propagation of Wave 2 through the nonlinear triad interactions among these waves and the mean zonal flow. The predominance of the periodic solution is consistent with frequent observations of such rather periodic variations of the Southern Hemisphere stratospheric polar vortex due to the triad interactions (Hio and Yoden 2004).

Vacillation in the presence of surface topography is complicated because of the modulation of the zonal mean zonal flow and wave amplitudes with the frequency of the Wave 2 phase propagation as described in Section 3. Detailed investigation of the transition from vacillation to periodic solution as the increase of r gives a deeper understanding of the periodic solutions in the presence of surface topography. The wave synchronization is explicitly shown in the polar diagrams of the complex amplitude of Wave 1 and 2 in Figs. 4 and 5. It was also diagnosed by the low-order "empirical mode expansion" in Section 4. The dependence of the spectral powers on r shown in Fig. 9 is well explained

by a limited number of nonlinear triad interactions among the zonal mean, Wave 1, and Wave 2 components, as summarized by Eqs. (28) $\sim$ (30) and (34) $\sim$ (36). These results are indicative of the usefulness of the low-order "empirical mode expansion" as a diagnosis tool. Refinement and application of such a method to study the variations of the polar vortex are interesting subjects for our future work. For example, if we could construct a low-order dynamical system based on such mode expansion, the diagnosis done in Section 4 would have a sound theoretical basis.

Acknowledgments. We appreciate the three anonymous reviewers for their helpful comments. The GFD-DENNOU library (SGKS Group 2001) was used for graphical output. This work was supported in part by the Grant-in-Aid for Scientific Research of the Ministry of Education, Culture, Sports, Science, and Technology (MEXT) of Japan, and by the Kyoto University Active Geosphere Investigations for the 21st Century COE (KAGI 21), which was approved by the MEXT of Japan.

REFERENCES

Baldwin, M., T. Hirooka, A. O'Neill and S. Yoden, 2003: Major stratospheric warming in the Southern Hemisphere in 2002: Dynamical aspects of the ozone hole split. *SPARC Newsletter*, **20**, 24-26.

Bernardet, P., A. Butet, M. D'equé, M. Ghil and R. L. Pfeffer, 1990: Low-frequency oscillations in a rotating annulus with topography. *J. Atmos. Sci.,* **47,** 3023-3043.

Hartmann D. L., 1983: Barotropic instability of the polar night jet stream. *J. Atmos. Sci.*, **40**, 817-835.

Hide, R., and P.J. Mason, 1975: Sloping convection in a rotating fluid. *Adv. Phys.*, **24**, 47-100.

Hio, Y., and I. Hirota, 2002: Interannual variations of planetary waves in the Southern Hemisphere stratosphere. *J. Meteor. Soc. Japan*, **80**, 1013-1027.

——, and S. Yoden, 2004: Quasi-periodic variations of the polar vortex in the Southern Hemisphere stratosphere due to wave-wave interaction. *J. Atmos. Sci.*, **61**, 2510-2527.

——, and ——, 2005: Interannual variations of the seasonal march in the Southern Hemisphere stratosphere for 1979-2002 and characterization of the unprecedented Year 2002. *J. Atmos. Sci.*, **62**, 567-580.

Ishioka, K., and S. Yoden, 1995: Non-linear aspects of a barotropically unstable polar vortex in a forced-dissipative system: Flow regimes and tracer transport. *J. Met. Soc. Japan*, **73**, 201-212.

Juckes, M. N., and M. E. McIntyre, 1987: A high-resolution one-layer model of breaking planetary waves in the stratosphere. *Nature*, **328**, 590-596.

Li, G. Q., R. Kung and R. L. Pfeffer, 1986: An experimental study of baroclinic flows with and without wave-two bottom topography. *J. Atmos. Sci.,* **42,** 433-471.

Lorenz, E. N., 1963: The mechanics of vacillation. *J. Atmos. Sci.,* **20,** 448-464.

Manney, G.L., T. R. Nathan, and J. L. Stanford, 1988: Barotropic stability of realistic stratospheric jets. *J. Atmos. Sci.*, **45**, 2545-2555.

——, C. R. Mechoso, L. S. Elson, and J. D. Farrara, 1991: Planetary-scale waves in the Southern Hemisphere winter and early spring stratosphere: Stability analysis. *J. Atmos. Sci.*, **48**, 2509-2523.

Mizuta, R., and S. Yoden, 2001: Chaotic mixing and transport barriers in an idealized stratospheric polar vortex. *J. Atmos. Sci.*, **58**, 2615-2628.

Prieto, R., and W. H. Schubert, 2001: Analytical predictions for zonally symmetric equilibrium states of the stratospheric polar vortex. *J. Atmos. Sci.*, **58**, 2709-2728.

Risch, S. H., and P. L. Read, 2005a: A laboratory study of global-scale wave interactions in baroclinic flow with topography I: basic flow regimes. *Geophys. Astrophys. Fluid Dyn.*, submitted.

——, and ——, 2005b: A laboratory study of global-scale wave interactions in baroclinic flow with topography II: vacillations and low-frequency variability.

Geophys. Astrophys. Fluid Dyn., submitted.

Rong, P. P., and D. W. Waugh, 2004: Vacillations in a shallow water model of the stratosphere. *J. Atmos. Sci.*, **61**, 1174-1185.

SGKS Group, cited 2001: DCL-5.2 (in Japanese). GFD-DENNOU Club. [Available online at http://www.gfd-dennou.org/library/dcl/.]

Shiotani, M., N. Shimoda, and I. Hirota, 1993∶Interannual variability of the stratospheric circulation in the southern hemisphere. *Quart. J. Roy. Meteor. Soc.*, **119**, 531-546.

Thuburn, J., and V. Lagneau, 1999: Eulerian mean, contour integral, and finite-amplitude wave activity diagnostics applied to a single layer model of the winter stratosphere. *J. Atmos. Sci.*, **56**, 689-710.

Yoden, S., 1983a: Nonlinear interactions in a two-layer, quasi-geostrophic, low-order model with topography. Part I: Zonal flow-forced wave interactions. *J. Met. Soc. Japan*, **61**, 1-18.

———, 1983b: Nonlinear interactions in a two-layer, quasi-geostrophic, low-order model with topography. Part II: Interactions between zonal flow, forced waves and free waves. *J. Met. Soc. Japan*, **61**, 19-35.

———, 1985a: Bifurcation properties of a quasi-geostrophic, barotropic, low-order model with topography. *J. Met. Soc. Japan*, **63**, 535-546.

———, 1985b: Multiple stable states of quasi-geostrophic barotropic flow over sinusoidal topography. *J. Met. Soc. Japan*, **63**, 1031-1045.

———, and K. Ishioka, 1993: A numerical experiment on the breakdown of a polar vortex due to forced Rossby waves. *J. Met. Soc. Japan*, **71**, 59-72.

Table 1: Regime diagram as a function of B and r. List of the symbols is given below. See text for details. The periodic solution for the parameters $B = 6.0°$ and $r = 0.08$ (denoted by P^*) was investigated in details in HY04. Regime transitions depending on r at $B = 4.0°$ (in bold characters) is examined in Section 3.2.

$r\backslash B$ [°]	3.0	3.5	**4.0**	4.5	5.0	5.5	6.0	6.5	7.0	7.5	8.0	9.0	10	11	12	$\cdots$
0.	V_0	V_0	$\boldsymbol{V_0}$	V_0	V_0	V_0	S	S	S	S	S	S	S	S	N	$\cdots$
0.02	V	V	$\boldsymbol{P}$	P	P	P	P	P	P	P	P	Sta	Sta	Sta	Sta	$\cdots$
0.04	P	P	$\boldsymbol{P}$	P	P	P	P	P	P	P	P	Sta	Sta	Sta	Sta	$\cdots$
0.06	P	P	$\boldsymbol{P}$	P	P	P	P	P	P	P	P	Sta	Sta	Sta	Sta	$\cdots$
0.08	I	I	$\boldsymbol{I}$	P	P	P	P^*	P	P	P	P	Sta	Sta	Sta	Sta	$\cdots$
0.10	I	I	$\boldsymbol{I}$	I	I	P	P	P	P	P	P	Sta	Sta	Sta	Sta	$\cdots$

N	no-wave sol.	
S	steady-wave sol.	$\psi_2(\lambda,\phi,t) = C_2(\phi)e^{i(2\lambda-\omega_P t)}$
V_0	vacillation sol.	$\psi_2(\lambda,\phi,t) = \{C_2(\phi) + A_2(\phi)e^{i\omega_A t}\}e^{i(2\lambda-\omega_P t)}$
Sta	stationary-wave sol.	$\psi_1(\lambda,\phi) = S_1(\phi)e^{i\lambda}$
P	periodic sol.	$\psi_1(\lambda,\phi,t) = S_1(\phi)e^{i\lambda} + \{C_1(\phi) + B_1(\phi)e^{i\omega_B t}\}e^{i(\lambda-\omega_B t)}$
		$\psi_2(\lambda,\phi,t) = S_2(\phi)e^{i2\lambda} + \{C_2(\phi) + B_2(\phi)e^{i\omega_B t}\}e^{i(2\lambda-\omega_B t)}$
V	vacillation sol.	(in the presence of surface topography)
I	irregular sol.	

Figure Captions

Figure 1 Time averaged structure of the eastward traveling Wave 2 (bottom right) and time evolution of its amplitude modulation component (other seven figures) for the vacillation solution with $B = 4^\circ$ and $r = 0$. The PV field is scaled by Ω and the contour interval is given by `cont`. Zero lines are not drawn and the areas where the value is smaller than $-$ `cont` are shaded.

Figure 2 (a) Time averaged structure of traveling Wave 2, (b) stationary Wave 1, and (c) traveling Wave 1 for the periodic solution with $B = 4^\circ$ and $r = 0.02$. Contour interval is given by `cont`. Zero lines are not drawn and the areas where the value is smaller than $-$ `cont` are shaded.

Figure 3 Time mean (denoted by dot) and variation range (vertical bar) of the zonal mean zonal flow (a), PV amplitude of the traveling Wave 2 (b), and that of Wave 1 (c) at 62.3°S plotted for the external parameter r with $B = 4^\circ$. Solid lines in (b) and (c) show the amplitude of stationary Wave 2 and 1, respectively. Downward arrows a - h at the top in panel (a) indicates the points shown in Figs. 4 and 6.

Figure 4 Time variation of the zonal mean zonal flow at 65.1°S (top), a polar diagram of the complex amplitude of Wave 2 at ϕ_2 (middle), and that of Wave 1 at ϕ_1 (bottom) for eight values of r (a - h) with $B = 4^\circ$. The latitude ϕ_s where the amplitude of the traveling wave of wavenumber s has its maximum is shown in each panel. The symbols ($\circ$) and ($+$) indicate the phase at the time when the zonal mean zonal wind reaches its local maximum and minimum, respectively.

Figure 5 Same as Fig. 4, but around the transition point. (a)$r = 0.0145$, (b)$r =$

0.01500, (c)$r = 0.01502$, and (d)$r = 0.01504$.

Figure 6 power spectral density for the time series of the zonal mean component of PV at $\phi = 62.3°$S [$\times\Omega^2$ day] (top), the amplitude of Wave 2 at $\phi = 62.3°$S (middle), and the Wave 2 component containing phase information at a point $(\lambda, \phi) = (0°, 62.3°\text{S})$ (bottom), for six values of r with $B = 4°$: (a) $r = 0$, (b) $r = 0.008$, (c) $r = 0.014$, (d) $r = 0.016$, (g) $r = 0.07$, and (h) $r = 0.09$.

Figure 7 Frequencies of the spectrum peak (top) and corresponding power spectral density (bottom) for only three components of f_A (plus sign), f_B (closed circle), and $f_A - f_B$ (diamond) which are obtained from the time series of (a) the zonal mean component, (b) the amplitude of Wave 2, and (c) the amplitude of Wave 1, of the relative vorticity at $\phi = 62.3°$S.

Figure 8 Same as Fig. 7 (bottom), but plotted on a double logarithmic chart. Only two components of f_A (plus sign) and f_B (closed circle) are shown.

Figure 9 Same as Fig. 7 (bottom) only for f_A component (plus sign), but plotted against $(r_b - r)$ on a double logarithmic chart for $r < r_b$.

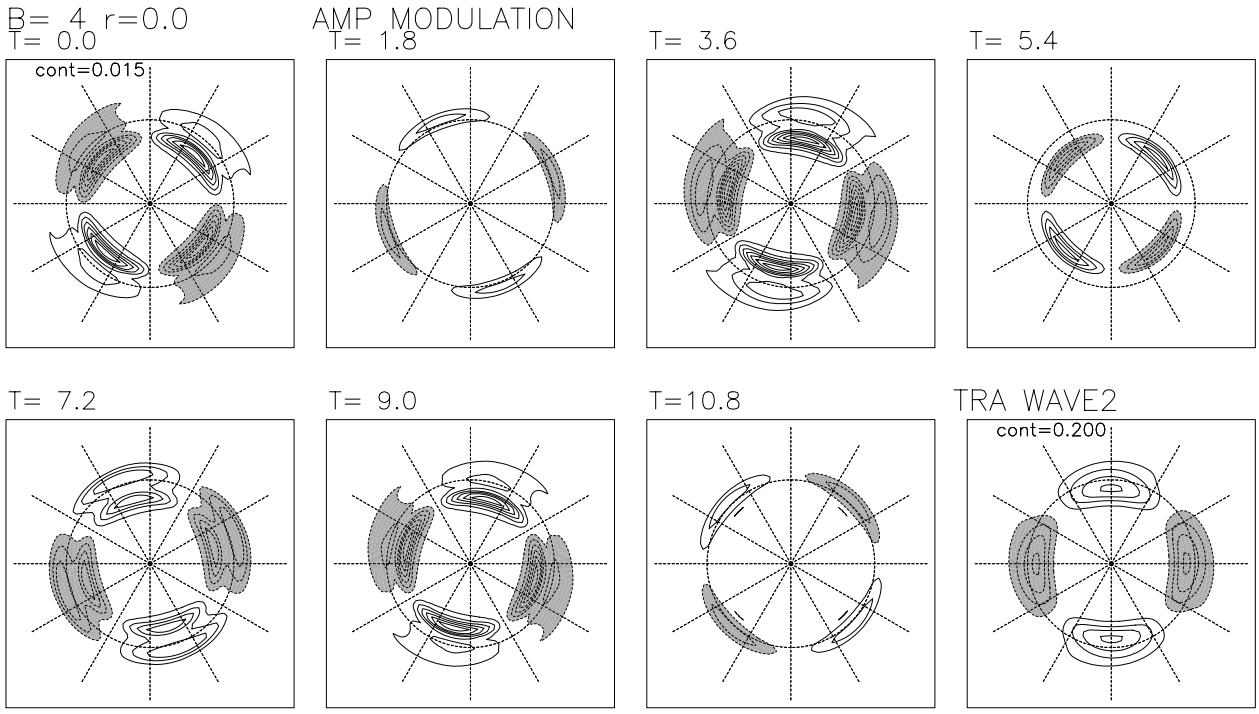

Figure 1: Time averaged structure of the eastward traveling Wave 2 (bottom right) and time evolution of its amplitude modulation component (other seven figures) for the vacillation solution with $B = 4°$ and $r = 0$. The PV field is scaled by Ω and the contour interval is given by `cont`. Zero lines are not drawn and the areas where the value is smaller than $-$ `cont` are shaded.

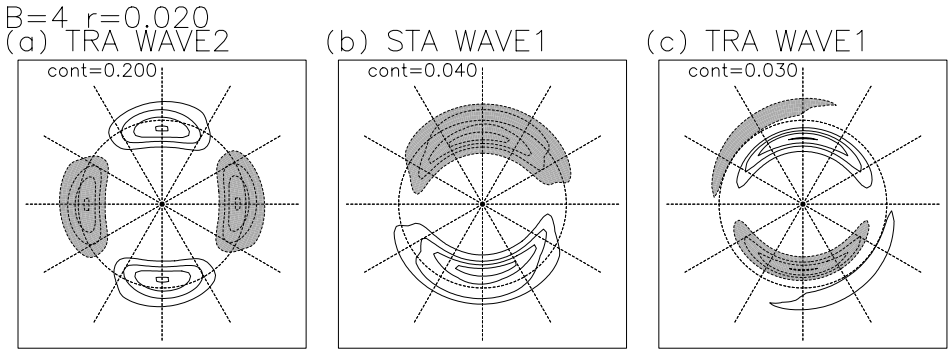

Figure 2: (a) Time averaged structure of traveling Wave 2, (b) stationary Wave 1, and (c) traveling Wave 1 for the periodic solution with $B = 4°$ and $r = 0.02$. Contour interval is given by `cont`. Zero lines are not drawn and the areas where the value is smaller than $-$ `cont` are shaded.

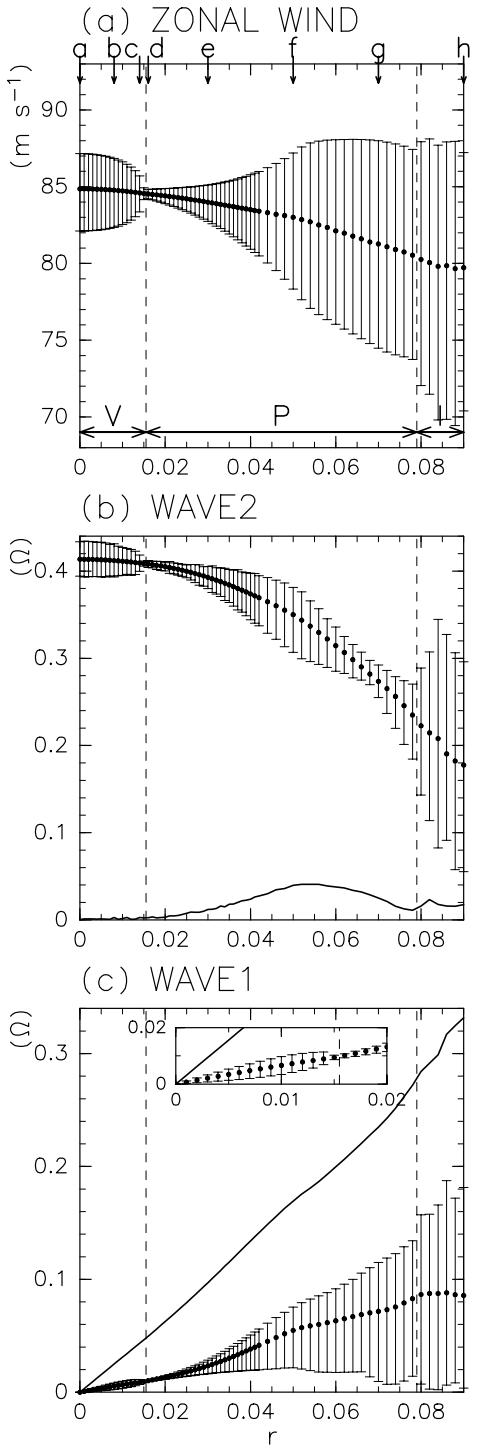

Figure 3: Time mean (denoted by dot) and variation range (vertical bar) of the zonal mean zonal flow (a), PV amplitude of the traveling Wave 2 (b), and that of Wave 1 (c) at 62.3°S plotted for the external parameter r with $B = 4°$. Solid lines in (b) and (c) show the amplitude of stationary Wave 2 and 1, respectively. Downward arrows a - h at the top in panel (a) indicates the points shown in Figs. 4 and 6.

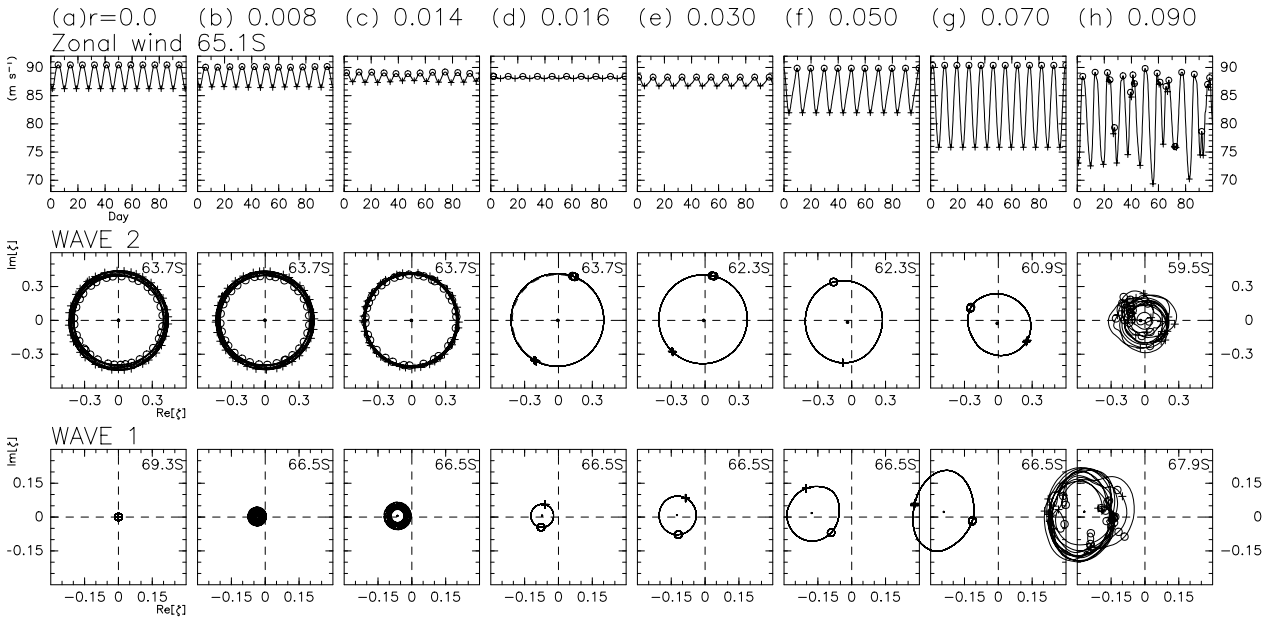

Figure 4: Time variation of the zonal mean zonal flow at 65.1°S (top), a polar diagram of the complex amplitude of Wave 2 at ϕ_2 (middle), and that of Wave 1 at ϕ_1 (bottom) for eight values of r (a - h) with $B = 4°$. The latitude ϕ_s where the amplitude of the traveling wave of wavenumber s has its maximum is shown in each panel. The symbols ($\circ$) and ($+$) indicate the phase at the time when the zonal mean zonal wind reaches its local maximum and minimum, respectively.

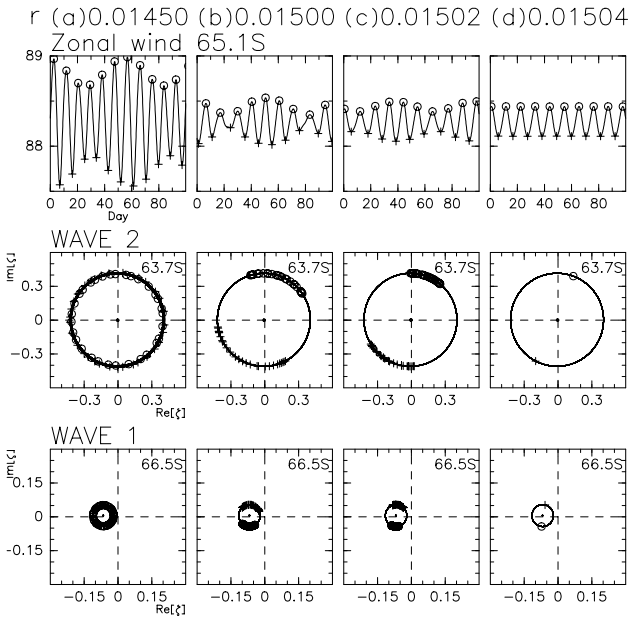

Figure 5: Same as Fig. 4, but around the transition point. (a)$r = 0.0145$, (b)$r = 0.01500$, (c)$r = 0.01502$, and (d)$r = 0.01504$.

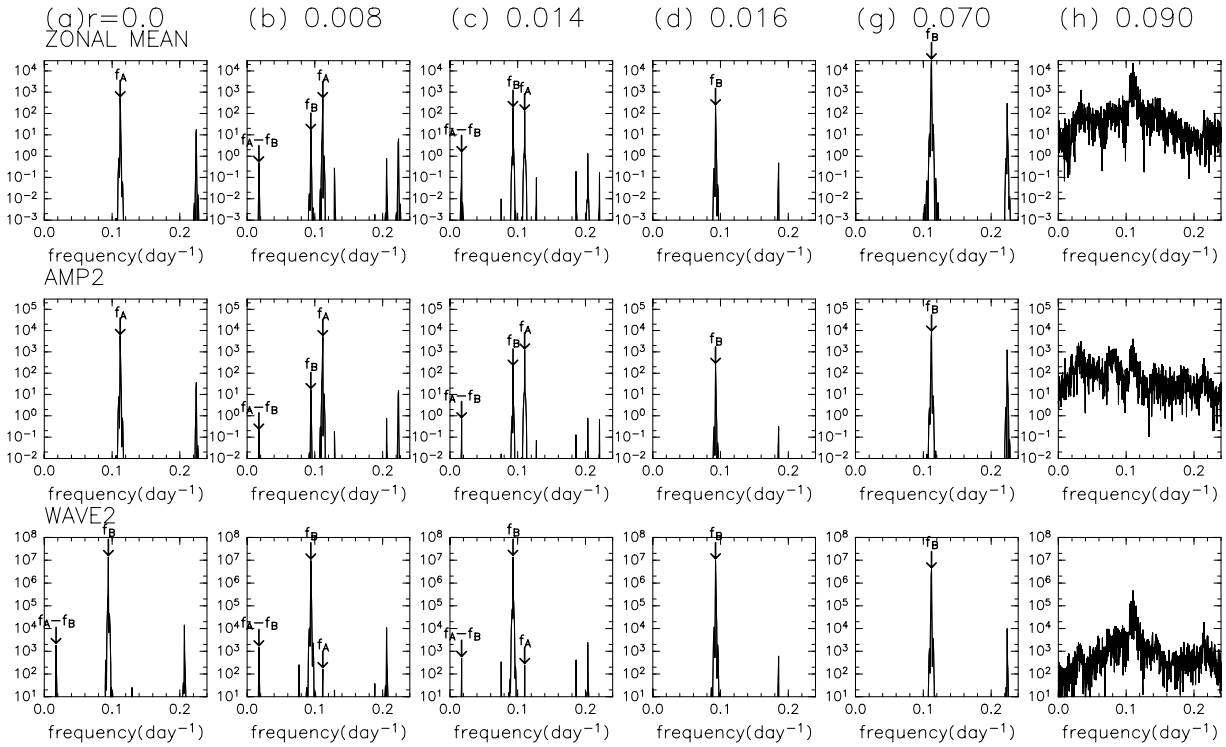

Figure 6: power spectral density for the time series of the zonal mean component of PV at $\phi = 62.3°\mathrm{S}$ [$\times\Omega^2$ day] (top), the amplitude of Wave 2 at $\phi = 62.3°\mathrm{S}$ (middle), and the Wave 2 component containing phase information at a point $(\lambda, \phi) = (0°, 62.3°\mathrm{S})$ (bottom), for six values of r with $B = 4°$: (a) $r = 0$, (b) $r = 0.008$, (c) $r = 0.014$, (d) $r = 0.016$, (g) $r = 0.07$, and (h) $r = 0.09$.

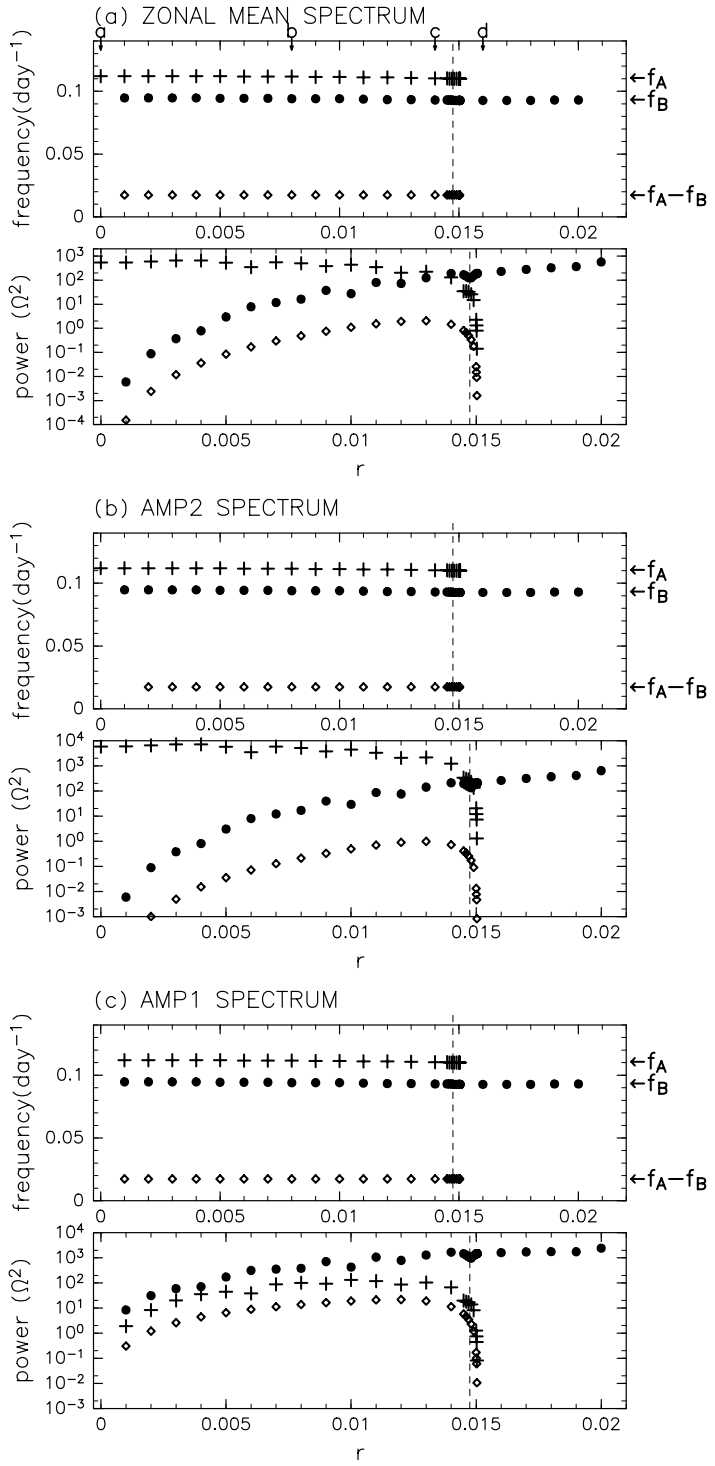

Figure 7: Frequencies of the spectrum peak (top) and corresponding power spectral density (bottom) for only three components of f_A (plus sign), f_B (closed circle), and $f_A - f_B$ (diamond) which are obtained from the time series of (a) the zonal mean component, (b) the amplitude of Wave 2, and (c) the amplitude of Wave 1, of the relative vorticity at $\phi = 62.3°$S.

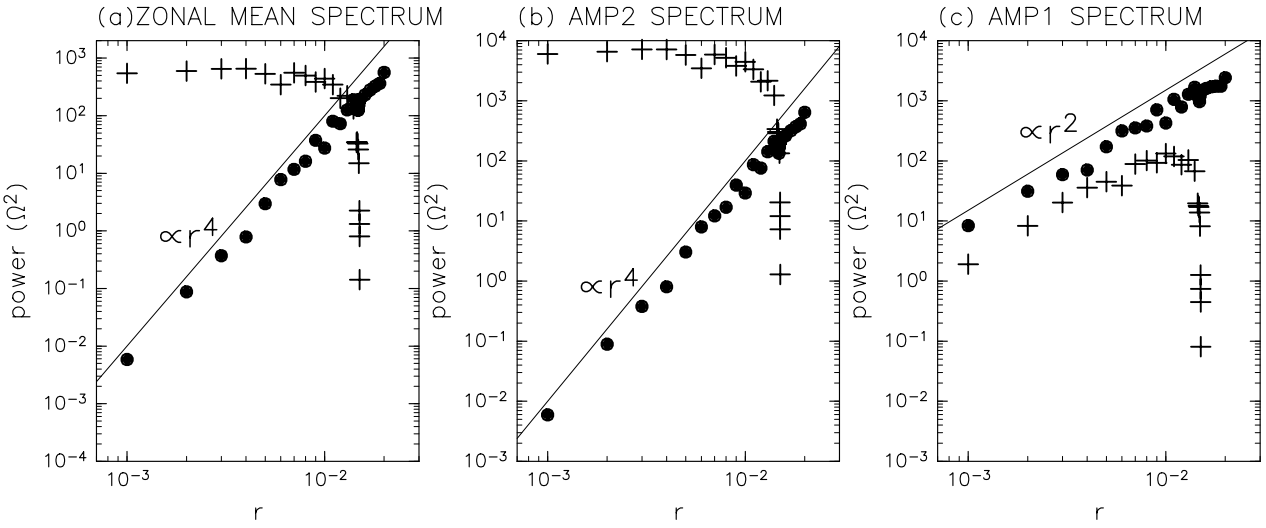

Figure 8: Same as Fig. 7 (bottom), but plotted on a double logarithmic chart. Only two components of f_A (plus sign) and f_B (closed circle) are shown.

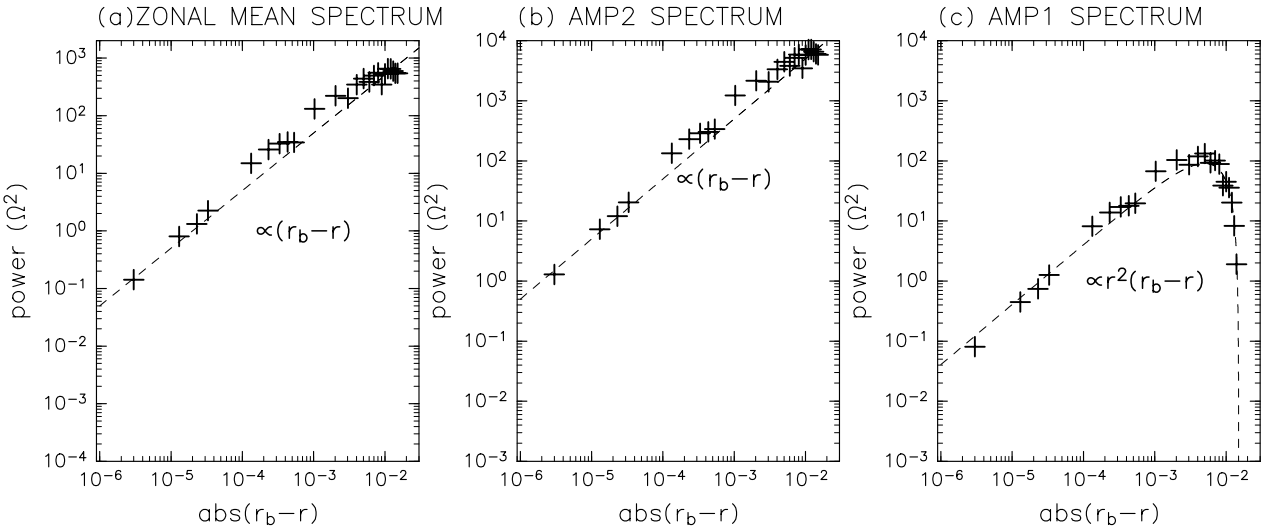

Figure 9: Same as Fig. 7 (bottom) only for f_A component (plus sign), but plotted against $(r_b - r)$ on a double logarithmic chart for $r < r_b$.